

CHANDRA OBSERVATIONS OF THE X-RAY POINT SOURCE POPULATION IN NGC 4636

JENNIFER POSSON-BROWN¹, SOMAK RAYCHAUDHURY², WILLIAM FORMAN¹, R. HANK DONNELLY^{1,3}, CHRISTINE JONES¹

Submitted to ApJ – May 2006

ABSTRACT

We present results on the X-ray point source population in the nearby Virgo elliptical galaxy NGC 4636 from four *Chandra* X-ray observations. These observations, totaling ~ 210 ks, were taken with the Advanced CCD Imaging Camera (ACIS) over a three year period. Using a wavelet decomposition detection algorithm, we detect 336 individual point sources. For our analysis, we use a subset of the 245 detections with ≥ 10 cts (a limiting luminosity of approximately 1×10^{37} erg s⁻¹ in the 0.5 – 2 keV band, outside the central 1.5' bright galaxy core). Of these sources, ~ 120 are likely members of NGC 4636, based on their distance from the center of the galaxy and the estimated AGN density of the field. The remaining sources are likely AGN. We examine, for the first time, variability over a period of years for X-ray point sources in an elliptical galaxy. Fifty-one sources (24%) in the common ACIS fields of view show significant variability between observations. Of these, 22 are detected with at least 10 counts in only one observation and thus may be “transient”. Of the 30 brightest sources whose lightcurves we examine over the course of a single observation, we find 4 (13%) that show short-term variability. We present a luminosity function for the point sources in NGC 4636, fit by a power-law with $\gamma = -1.24 \pm 0.04$, as well as a radial source density profile, hardness ratios for the sources, and lightcurves for bright sources which display short-term variability. We find an upper limit to the current X-ray luminosity of the historical supernova SN1939A. We find 102 matches between our X-ray point sources and potential globular cluster (GC) candidates found in deep optical images of NGC 4636. In the annulus from 1.5' to 6' of the galaxy center, 50 of the 114 X-ray point sources (44%) with ≥ 10 counts are matched with GC candidates brighter than $R < 23.5$. Since we expect 20% of these sources to be background AGN, the percentage matched with GCs could be as high as 55%. Of these 50 sources, we find that $\sim 80\%$ are associated with the redder GC candidates, those that are thought to have near-solar metal abundance. However, we do not find a correlation between the detection of X-ray point sources and the luminosity of the host GC candidate. The luminosity functions of the point sources matched with GCs and of those that are unmatched reveal similar underlying populations. Finally, we present a color-color diagram based on ratios of X-ray flux rather than source counts, which yields a much tighter distribution, and shows a large population of sources which are likely LMXBs and a small population of black hole candidates.

Subject headings: galaxies: individual (NGC 4636) — X-rays: galaxies — X-rays: binaries

1. INTRODUCTION

The sub-arcsecond resolution of the *Chandra* Observatory has revealed the nature of X-ray emitting point sources in nearby galaxies. It is clear that almost all the very luminous ($L_x > 10^{36}$ erg s⁻¹) point sources in galaxies belong to two distinct populations of compact stars, their evolutionary timescales depending upon that of their donor companions: the low-mass X-ray binaries (LMXB), which are long-lived and evolve on timescales of 10^9 – 10^{10} yr, and high-mass X-ray binaries (HMXB), which evolve on timescales of 10^6 – 10^7 yr. The latter population is thus an indicator of recent star formation and is not expected to be found in early-type galaxies, unless a recent merger has occurred. The LMXB population, on the other hand, has lifetimes comparable with that of the host galaxy, and their number and combined luminosity is found to correlate well with the stellar mass of galaxies (Gilfanov 2004).

In this paper, we present a *Chandra* view of the X-ray point source population of NGC 4636, a bright E/S0 galaxy on the southern periphery of the Virgo cluster. It has a radial velocity similar to that of Virgo, but is 10.8° from the center of the cluster, which corresponds to 2.8 Mpc at a distance of 15 Mpc (Tonry et al. 2001). Furthermore, the galaxy lies at the center of a poor group (Osmond & Ponman 2004; Miles et al. 2004), possibly falling into the cluster. Its unusual properties have attracted detailed multiwavelength research for several decades. NGC 4636 has an anomalously large specific frequency of globular clusters (Dirsch et al. 2005), comparable to that of central cluster galaxies like NGC 1399 (Dirsch et al. 2003). It has been suggested that the galaxy has an unusually large dark halo (Loewenstein & Mushotzky 2003). NGC 4636 was one of the first early-type galaxies in which neutral hydrogen was detected (Knapp et al. 1978), and further radio observations (Birkinshaw & Davies 1985) revealed a weak central radio source and small-scale jets. Its far-infrared luminosity greatly exceeds that expected from its stellar content (Temi et al. 2003), and the luminosity in the vicinity of 100μ is consistent with dust emission from a recently accreted disk galaxy. Its flattened (E4) morphology at the outer faint isophotes (Sandage 1961) indicates the presence of large-scale angular momentum, often associated with recent mergers.

NGC 4636 is one the brightest nearby early-type galaxies in X-rays, and so it has been well-studied with generations of

¹ Smithsonian Astrophysical Observatory, Harvard-Smithsonian Center for Astrophysics, 60 Garden Street, Cambridge, MA 02138

² School of Physics and Astronomy, University of Birmingham, Edgbaston, Birmingham B15 2TT, United Kingdom

³ Center for Naval Analysis, 4825 Mark Center Drive, Alexandria, VA 22311

Electronic address: jpossonbrown@cfa.harvard.edu

Electronic address: somak@star.sr.bham.ac.uk

Electronic address: wforman@cfa.harvard.edu

Electronic address: cjones@cfa.harvard.edu

X-ray observatories. It was first detected as an extended X-ray source by *Einstein* (Forman et al. 1985). ROSAT and ASCA observations found abundance and temperature gradients in its extended X-ray halo (Trinchieri et al. 1994; Matsushita et al. 1997, Buote 2000), while *Chandra* and XMM-Newton observations (Jones et al. 2002; O’Sullivan et al. 2005) show symmetric arm features and cavities in the extended X-ray halo, interpreted to be evidence of past AGN activity.

We introduce the observations and discuss data reduction and point source detection in §2. In §3.1, we examine the distribution of sources in NGC 4636 and present a luminosity function for the galaxy. In §3.2, we use soft, medium, and hard band source fluxes to make an X-ray color-color diagram which is independent of any instrumental or detector effects. In §3.3, we examine the X-ray point source population to look for variable sources on both long and short timescales. In §3.4, we optically identify sources associated with globular clusters and show a color histogram of these sources. In §3.5, we examine a few interesting individual sources detected in our observations. Finally, our analysis and results are summarized in §4.

2. OBSERVATIONS, DATA PROCESSING, AND POINT SOURCE DETECTION

The observations presented in this paper were made with the ACIS-I and ACIS-S detectors on *Chandra* on four occasions spanning three years. The observations are summarized in Table 1.⁴ The FOV of each observation is overlaid onto an optical DSS image in Figure 1.

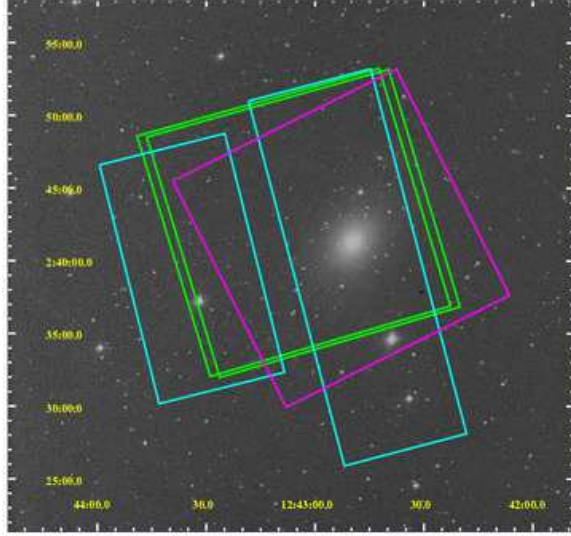


FIG. 1.—A DSS optical image of NGC 4636 with the FOV of our *Chandra* observations overlaid. The magenta outline is the December 1999 ACIS-I observation, the light blue outline is the January 2000 ACIS-S observation, and the green outlines are the February 2003 ACIS-I observations.

We obtained level 1 event lists for the observations from the *Chandra* data archive. We filtered these event lists to include only those events with “good” grades (i.e. 0,2,3,4 and 6) and to exclude bad pixels. The event lists were also filtered

⁴ The short (5 ks) ACIS-I observation (sequence #600084) yielded no sources that were not detected in the other observations, and the source counts in the few detections present in this observation were too low to allow meaningful analysis. Thus, we do not use this observation in the work discussed in the remainder of the paper.

TABLE 1
SUMMARY OF *Chandra*/ACIS OBSERVATIONS OF NGC 4636

Date	Detector	Sequence #	Exposure Time (s)
1999 Dec 5	ACIS-I	600084	4858
2000 Jan 26	ACIS-S	600083	44450
2003 Feb 14	ACIS-I	600300	74709
2003 Feb 15	ACIS-I	600331	74190

on the nominal good time intervals for each observation. Additional time filtering was done to remove times affected by background flaring. The remaining total good exposure times are listed in Table 1.

We created a 0.5 – 2 keV band image for each observation and used the wavelet decomposition algorithm *wvdecomp* (Vikhlinin et al. 1995) on the images to detect sources. In addition, we co-added the two ACIS-I observations done sequentially in February 2003, and ran the source detection algorithm on this image. After detection, source locations were refined using a centroiding algorithm, and the 90% encircled energy radius, based on the preflight calibration model of the *Chandra* PSF, was determined for each source location.

For each observation, we constructed a 0.5 – 2 keV band background image by summing the large-scale wavelet decompositions. For each source, we made a background region centered on the source location and scaled the radius so that the background region contained at least 64 counts. We also made an exposure map for each observation. For each source detected in each observation, we tabulated raw and net (i.e. background-subtracted) counts, and raw and net exposure-corrected counts. We compared source positions between the observations, and matched sources whose coordinates agree by less than 2''.

As a final step in the initial analysis, we calculated a counts-to-flux conversion factor for each source by computing response matrices at each source location in the appropriate ACIS chip, assuming a power-law model with $\Gamma = 1.5$ and $n_H = 1.81 \times 10^{20} \text{ cm}^{-2}$. (After comparing fluxes computed with conversion factors based on different values of Γ and n_H , we conclude that the choice of parameter values, within a reasonable range, does not significantly impact the resulting fluxes in each band. Even choosing a large value, such as $\Gamma = 3$, changes the resulting fluxes by less than 20%.) To convert source fluxes to luminosities, we assume a distance of $d = 15 \text{ Mpc}$.

From the 0.5 – 2 keV background images, we estimate the luminosity a source would need to have to be detected at a given location. By looking at the maximum values of these “ S_{min} ” maps, we estimate that outside of the bright 1.5' central core, our source detection is complete above $\sim 1.7 \times 10^{37} \text{ erg s}^{-1}$. Of the 245 sources that we detect with ≥ 10 net counts, 201 are above this luminosity.

A summary of X-ray point sources detected in the NGC 4636 observations with at least 10 net counts is given in Table 2.

3. RESULTS

3.1. Point Source Distribution and Luminosity Function

The radial X-ray source density profile for NGC 4636 is shown in Figure 3. From results of the *Chandra* Deep Fields (Bauer et al. 2004), we estimate an AGN density of ~ 0.3

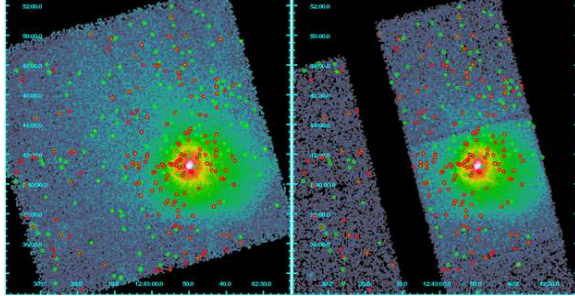


FIG. 2.— Smoothed, exposure-corrected images in the 0.5 – 2 keV range. North is up and East is to the left. The left image is from the co-added ACIS-I observations taken in February 2003, totaling approximately 150 ks. The right image is from the 50 ks ACIS-S observation taken in January 2000. Green circles show sources detected in the ACIS-I image and red circles show sources detected in the ACIS-S image. Sources detected in the ACIS-I observations lying outside of the ACIS-S FOV are not shown on the ACIS-S image.

arcmin⁻² at our limiting flux of $\sim 4 \times 10^{-16}$ erg cm⁻² s⁻¹ in the 0.5 – 2 keV band. Based on this estimate, our field becomes AGN-dominated beyond $\sim 6'$ of the galaxy center. Between 1.5' and 6', we estimate that 20% of our sources are AGN and 80% are LMXB.

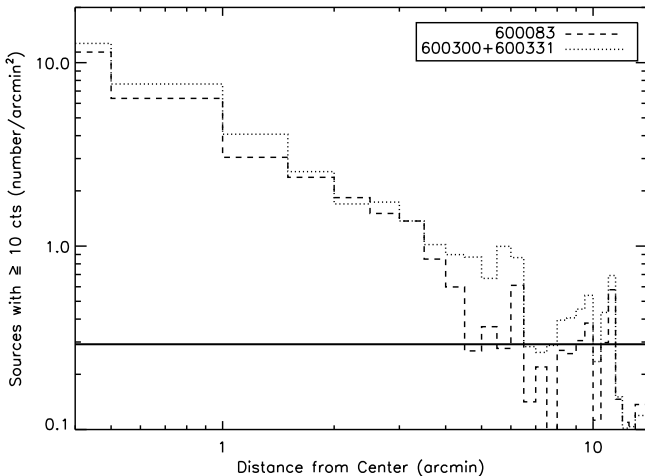


FIG. 3.— Radial source density profile for sources with ≥ 10 counts. The ACIS-S observation (sequence # 600083) is shown by a dashed line and the sequential co-added ACIS-I observations (600300 and 600331) are shown with a dotted line. From results of the *Chandra* Deep Fields (Bauer et al. 2004), we estimate an AGN density of ~ 0.3 arcmin⁻² at our limiting flux of $\sim 4 \times 10^{-16}$ erg cm⁻² s⁻¹ in the 0.5 – 2 keV band. This density is shown by the solid line. Note that our field becomes AGN-dominated outside of $\sim 6'$.

Figure 4 shows the luminosity function in the 0.5 – 2 keV band for X-ray point sources in NGC 4636 lying between 1.5' and 6' from the center of the galaxy. Fitting the luminosity function with a power-law gives a best fit value of $\gamma = -1.24 \pm 0.04$. We see no evidence for a break in the luminosity function. Jordán et al. (2004) demonstrate that there is no compelling evidence for a break in the luminosity functions of other Virgo cluster galaxies such as M87, M49, or NGC 4697. Thus, we did not attempt fitting a broken power-law.

3.2. Spectral Analysis

Traditionally, X-ray colors are calculated as ratios of counts in different energy bands (e.g. Swartz et al. 2004; Prestwich et al. 2003). However, since we want to directly compare sources observed by X-ray detectors with different responses

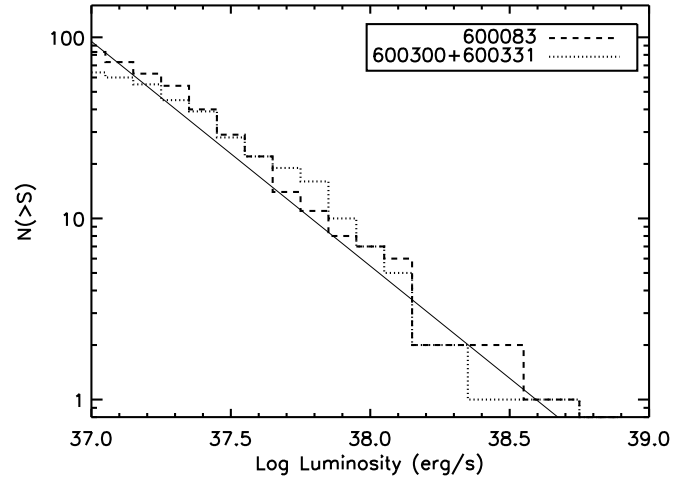


FIG. 4.— Luminosity function of X-ray point sources in NGC 4636 detected in the 0.5 – 2 keV band. Only sources with ≥ 10 counts and distance $1.5' < d < 6'$ from the center of the galaxy are included. The solid line shows a power-law with $\gamma = -1.24 \pm 0.04$.

(i.e. the ACIS-S and ACIS-I) and on different parts of the detector, we convert source counts to fluxes before computing X-ray colors. To do this, we found the counts-to-flux conversion factor for each source individually, as described at the end of §2, for three energy bands: soft (0.5 – 1 keV), medium (1 – 2 keV), and hard (2 – 8 keV). We then calculated one color as $C_1 = (\text{medium-soft})/\text{total}$ and another as $C_2 = (\text{hard-medium})/\text{total}$, as defined in Swartz et al. (2004). The resulting color-color diagram is shown in Figure 5. The plotting symbol size is proportional to the 0.5 – 2 keV band luminosity. We identify two distinct populations: a large cluster of harder, less luminous sources with power-law indices between 1 and 2, and a smaller group of softer, more luminous sources ($L_x \approx 10^{38}$ erg s⁻¹) with steeper power-law indices. Points in black lie less than 6' from the center of the galaxy and are most likely members, while points in red lie further than 6' from the center. The source represented by a black asterisk is located at the galactic nucleus, and the two sources with steep spectra represented by black triangles lie within 6'' of the nucleus. These may be signatures of black holes (see §3.5.1 and §3.5.2). The three red points clustered by the asterisk in Figure 5 are probably not members of NGC 4636, based on their distances from the galaxy center (all $> 6'$). They are very luminous ($L_x > 10^{38}$) and show long-term variability. Two of these sources are associated with GCs.

Figure 6 shows a color-color diagram based on counts for the same set of sources shown in Figure 5. We note that the flux-based diagram has much less scatter, making it easier to identify populations and trends.

3.3. Temporal Variability

We present a comparison of source fluxes between the January 2000 ACIS-S observation and co-added February 2003 ACIS-I observations in Figure 7. To search for long-term variable sources, we determine a significance threshold as

$$\frac{|flux_{Jan00} - flux_{Feb03}|}{\sqrt{flux_err_{Jan00}^2 + flux_err_{Feb03}^2}} > 3 \quad (1)$$

For the 214 sources in the common field of view detected with ≥ 10 net counts in at least one of the observations, we find 51 ($\sim 24\%$) are long-term variable sources. These are shown in

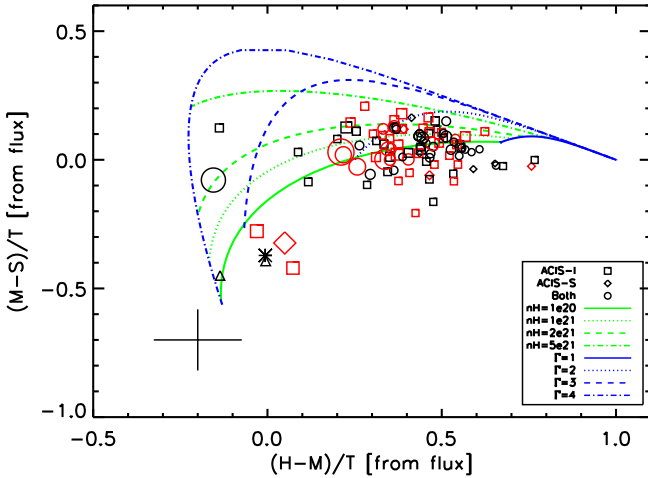


FIG. 5.— Color-color diagram of all point sources in the NGC 4636 observations having at least 5 net counts in each of the three bands. We follow the example of Swartz et al. (2004) and use bands $S = 0.5 - 1$ keV, $M = 1 - 2$ keV, and $H = 2 - 8$ keV ($T = S + M - H$, i.e. $0.5 - 8$ keV). Note, however, that these color ratios are calculated from source *flux*, as opposed to counts. This allows us to compare ACIS-I and ACIS-S directly. The different plotting symbols indicate whether the source was detected in the ACIS-I observation (open square), the ACIS-S observation (open diamond) or both observations (open circle). The asterisk denotes a source detected at the galaxy nucleus (see §3.5.1) and the two triangles denote blackhole candidates detected near the nucleus (see §3.5.2). Plotting symbol size is proportional to source luminosity in the $0.5 - 2$ keV band. Sources in red lie further than $6'$ from the center of the galaxy. The three red points near the asterisk are bright ($L_x > 10^{38}$), long-term variable sources, two of which are associated with GCs. Blue curves denote colors of absorbed power-law models of spectral indices $\Gamma = 1, 2, 3$, and 4 over the range of absorbing columns $n_H = 10^{20}$ to 10^{24} cm $^{-2}$. Green curves denote constant absorption columns, as given in the legend. A typical error bar is shown in the lower left corner.

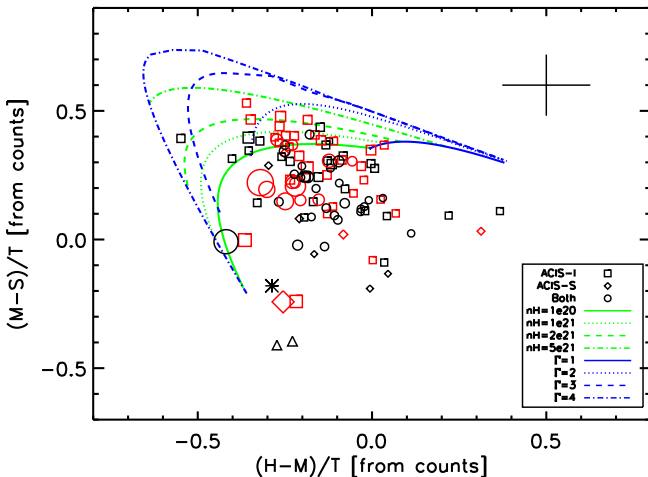


FIG. 6.— As in Figure 5, only here the colors are calculated from counts, whereas in Figure 5 they are calculated from fluxes. Note that here, unlike in Figure 5, it is not possible to easily group the sources into two populations. Although the ranges for the colors differ between this figure and Figure 5, the vertical and horizontal axes are 1.6 units long in both plots.

red in Figure 7 and are marked with a “V” in the last column of Table 2. Of these 51 sources, 29 have ≥ 10 counts in both observations, and the remaining 22 are “transient”. (That is, they have ≥ 10 counts in only one observation, and are not reliably detected in the other observation.) Of these 22 transient sources, 17 have ≥ 20 counts in only one observation, and < 10 counts in the other observation.

Similarly, to measure variability on shorter timescales, we

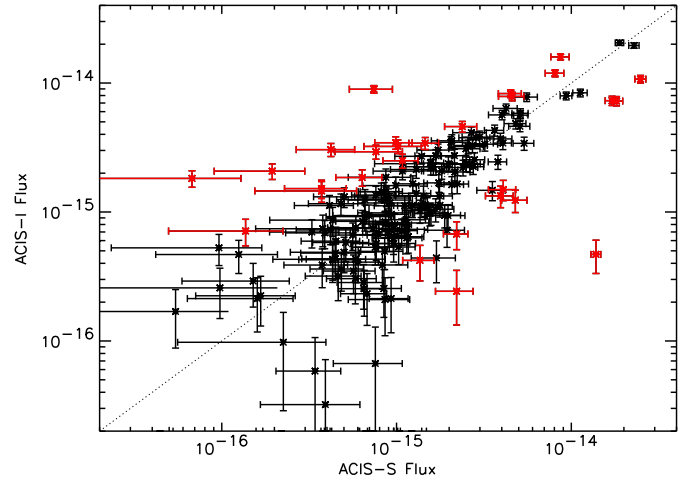


FIG. 7.— A comparison of source fluxes in the $0.5 - 2$ keV band from the 45 ks ACIS-S observation and co-added February 2003 ACIS-I observations. Only sources with ≥ 10 counts in each observation are plotted here. Variable sources are shown in red.

compare fluxes between the two February 2003 ACIS-I observations in Figure 8. These observations were done successively, each lasting for ~ 75 ks (~ 21 hrs). Out of 87 sources, we find four ($\sim 5\%$) whose fluxes vary by 3σ between the two observations; these are shown in red in Figure 8. Thus, a much larger percentage (24%) of sources display variability on a timescale of years (that is, between the January 2000 ACIS-S observation and the February 2003 ACIS-I observations) than on a timescale of days (i.e. between the two ACIS-I observations).

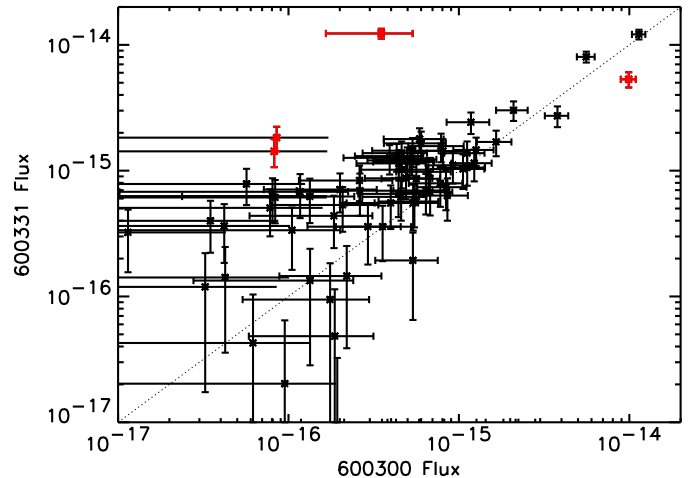


FIG. 8.— A comparison of source fluxes in the $0.5 - 2$ keV band from the 2003 February 14 75 ks ACIS-I observation (sequence number 600300) and the 2003 February 15 75 ks ACIS-I observation (600331). Only sources with ≥ 4 counts in each observation are plotted here. Variable sources are shown in red.

To search for variability on the timescale of hours (i.e. during a single observation), we examine the lightcurves of the 30 sources detected with 80 or more net counts, binning by 2000 ks, and use the χ^2 test to look for significant variations. We find four variable sources (13%), two of which lie within $6'$ of the galaxy’s center. Light-curves for these sources are shown in Figures 9 - 12, and these sources are marked with “SV” in the last column of Table 2. The first of these sources, a bursting X-ray source, is discussed further in §3.5.4.

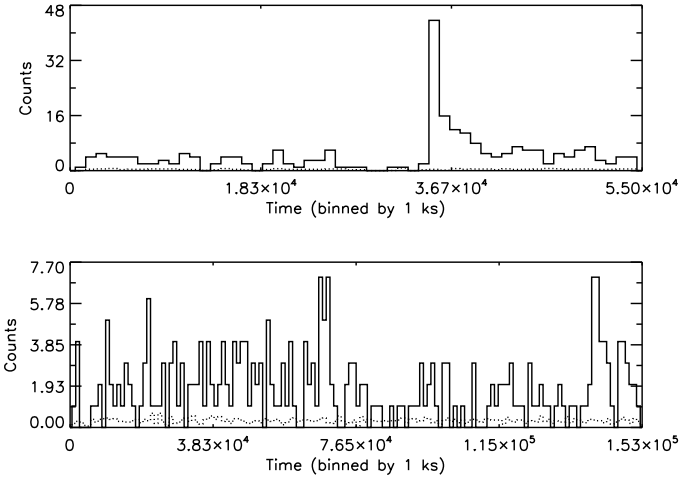


FIG. 9.— Variable source detected at $\alpha(J2000) = 190.8821^\circ$, $\delta(J2000) = 2.6193^\circ$. Counts are in the 0.5–2 keV band. Background counts are plotted with a dotted line. The upper panel is from the ACIS-S observation (sequence # 600083) and the lower panel is from the co-added ACIS-I observations (sequence #s 600300 and 600331). This source is discussed in §3.5.4.

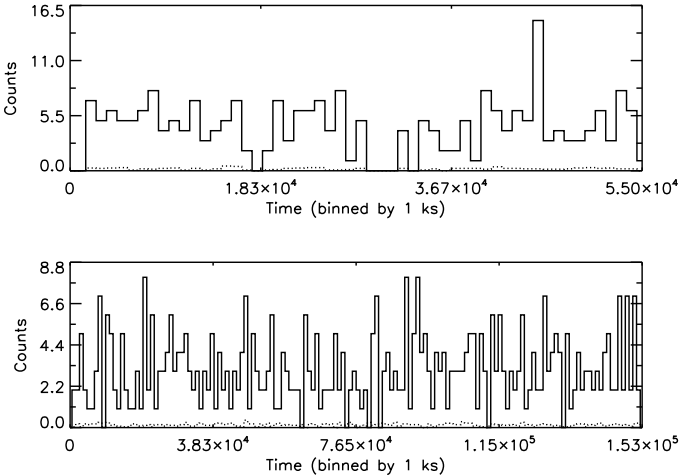


FIG. 10.— Variable source detected at $\alpha(J2000) = 190.7304^\circ$, $\delta(J2000) = 2.8324^\circ$. Counts are in the 0.5–2 keV band. Background counts are plotted with a dotted line. The upper panel is from the ACIS-S observation (sequence # 600083) and the lower panel is from the co-added ACIS-I observations (sequence #s 600300 and 600331).

3.4. Correlation with the globular cluster population

It is well-known that a significant fraction of LMXBs in the Milky Way and elsewhere is associated with globular clusters. In the Milky Way, $\sim 10\%$ of all bright ($> 10^{36} \text{ erg s}^{-1}$) LMXBs are found in globular clusters (GCs) (e.g. Grindlay 1993), even though GCs account for $< 10^{-3}$ of the stellar mass of the galaxy. This has led to the belief that LMXBs are very close binary systems formed as a result of dissipative two-body encounters between neutron stars and ordinary stars, which are more likely in the dense cluster cores (Fabien et al. 1975; Hut et al. 1992). Indeed, it has been suggested that LMXBs are formed primarily in this way in the cores of globular clusters, and some of the resulting binaries are later ejected from their host clusters (White et al. 2002). If so, one expects a direct correlation between the X-ray point source population corresponding to LMXBs and the globular cluster population in galaxies.

In early-type galaxies, *Chandra* observations show that

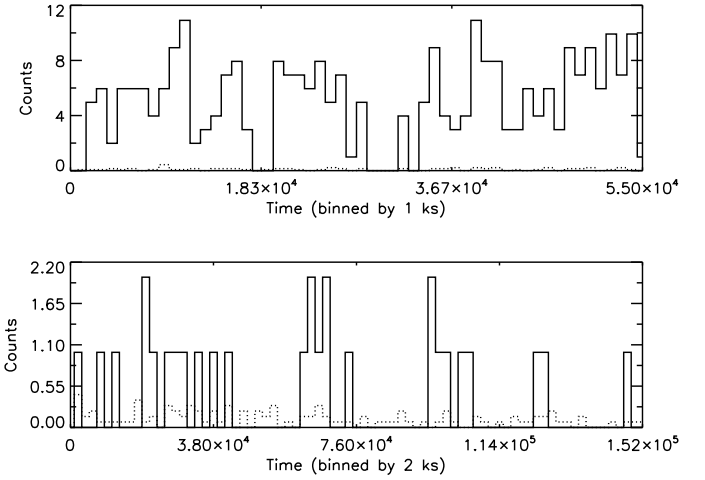


FIG. 11.— Variable source detected at $\alpha(J2000) = 190.7498^\circ$, $\delta(J2000) = 2.6591^\circ$. Counts are in the 0.5–2 keV band. Background counts are plotted with a dotted line. The upper panel is from the ACIS-S observation (sequence # 600083) and the lower panel is from the co-added ACIS-I observations (sequence #s 600300 and 600331).

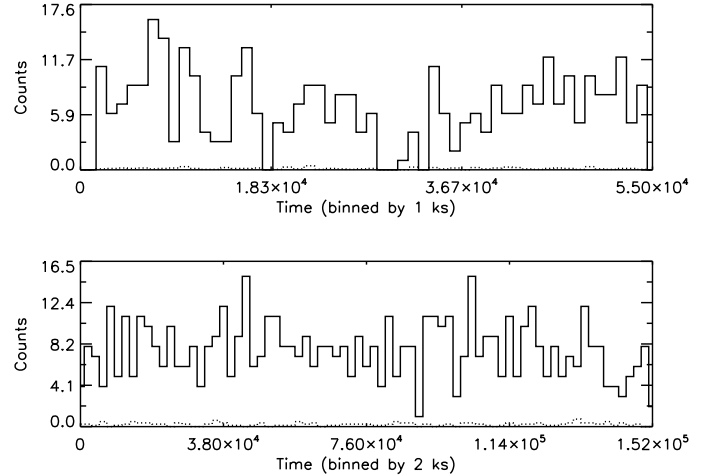


FIG. 12.— Variable source detected at $\alpha(J2000) = 190.7204^\circ$, $\delta(J2000) = 2.6303^\circ$. Counts are in the 0.5–2 keV band. Background counts are plotted with a dotted line. The upper panel is from the ACIS-S observation (sequence # 600083) and the lower panel is from the co-added ACIS-I observations (sequence #s 600300 and 600331).

there is an association of LMXBs with globular clusters. The fraction of LMXBs identified with known GCs varies from at least 20% in NGC 4697 (Sarazin et al. 2001) to up to 70% in NGC 1399, the central galaxy of the Fornax cluster (Angelini et al. 2001). Furthermore, it is observed that the LMXBs in early-type galaxies are > 3 times more likely to be in the redder globular clusters, for galaxies which exhibit bimodality in color of the GCs, e.g. M87 (Jordán et al. 2004) and NGC 4472 (Kundu et al. 2002). Since the redder GCs are thought to be relatively more metal-rich, this can be a diagnostic of the characteristics of the compact object’s companion star in the LMXB, and its history of formation (Maccarone et al. 2004; Ivanova 2006).

We matched our list of X-ray point sources with the list of globular cluster candidates from a deep mosaic CCD observation using the CTIO Blanco telescope from Dirsch et al. (2005). The photometry is available in the Washington C and R system. Of the optical point sources listed in this work which extend over an area of 0.25 deg^2 around the galaxy,

we chose the sources with magnitude $R < 23.5$ and color $0 < C-R < 2.5$ as globular cluster candidates. These are not spectroscopically confirmed to be globular clusters belonging to the galaxy; some could indeed be background galaxies. Figure 13 shows the distribution of both X-ray and optical point sources, together with other background sources that are known in the field. In a more recent paper, the group responsible for the original list has published spectral observations of a small subset of 200 of the original list of GC candidates (Schuberth et al. 2006). Of the sources with magnitude $R < 23.5$ and color $0 < C-R < 2.5$, >80% of the candidates were found to be globular clusters from measured redshift and the rest foreground stars.

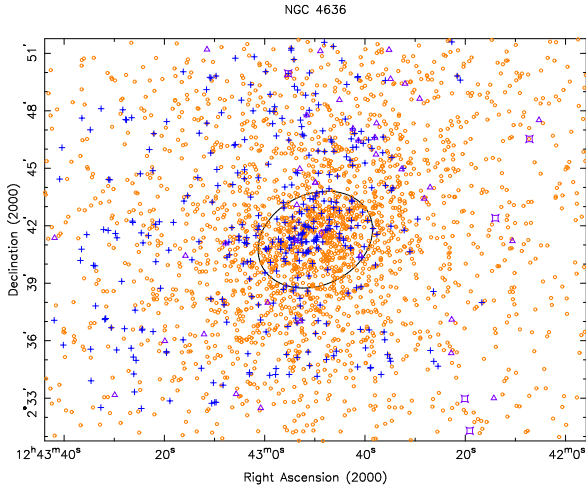


FIG. 13.— The X-ray point sources detected in NGC 4636, shown by '+'s, plotted along with all globular cluster candidates (discrete optical sources from Dirsch et al. (2005), brighter than $R < 23.5$), plotted as open circles. The optical extent of the galaxy is shown as the D_{25} ellipse (major and minor axis of $6.0'$ and $4.7'$ respectively). Other known optical sources (from NED) in the field are also plotted: quasars as squares, and background galaxies and clusters as triangles. The supernova remnant SN1939A is plotted as a diamond within the optical extent of the galaxy.

The positions of both X-ray and optical sources are known to an accuracy of better than an arcsecond. We matched the two lists by taking each X-ray point source, and finding its offset from the nearest globular cluster candidate. We checked for systematic translation and rotation between the two lists by seeking to maximize the matches for small values of rotation and translation of all sources, but could not improve upon the matching done in the above way. Based on the distribution of offsets, we chose to limit the search radius to $1.5'$. If two GC candidates fell within this radius, we assigned the X-ray source to the nearest one in angular distance. Of the 336 sources in our list, 102 were matched to globular cluster candidates. These sources are marked “GC” in the last column of Table 2 and are listed separately in Table 3. Of these 102 matched point sources, 50 lie within $1.5' < r < 6.0'$ of the center of NGC 4636 and have more than 10 raw counts in either of the Sequence 600083 or combined 600300 & 600331 observations. Based on the number of X-ray sources and GC candidates in this annulus, we expect only three chance coincidences. None of the other known background sources from NED were matched within the inner $10'$ from the center of the galaxy.

A $C-R$ color histogram of globular cluster candidates is shown in Figure 14. Like in many other early-type galaxies, the distribution of the colors of candidate globular clusters

here is bimodal, with peaks at $C-R = 1.28$ and 1.77 . It is believed that the difference in color between the two populations is due to a difference in metal abundance (e.g. Yoon et al. 2006), the redder GCs being of near-solar abundance. In NGC 4636, even though bluer GCs are more abundant, a majority of the X-ray point sources (LMXBs) are associated with the redder GCs, as is shown by the solid histogram, which represents the color distribution of the GCs matched with X-ray point sources. This is consistent with the observation that most Galactic LMXBs associated with GCs lie in those systems with a near-solar abundance (Bregman 2006).

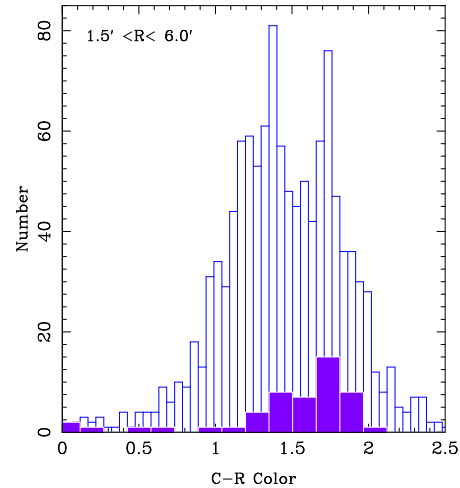


FIG. 14.— A histogram of all globular cluster candidates (discrete optical sources from Dirsch et al. (2005), brighter than $R < 23.5$), found within $1.5' < r < 6.0'$ of the center of NGC 4636, plotted along with those that match with X-ray point sources detected in the *Chandra* observations (solid histogram). It is clear that the X-ray point sources are preferentially associated with the redder globular clusters.

Other studies have found that X-ray point sources are preferentially found in optically more luminous globular clusters (Angelini et al. 2001; Sarazin et al. 2003). Such a correlation can be expected since one of the stars in an LMXB is a normal star, and brighter GCs have a higher number of potential companion stars in the binary. In Figure 15, we plot the apparent magnitude and color of the host globular clusters against the X-ray luminosity of the matched X-ray point sources. We do not find any trend with host GC luminosity, while, as noted before, the correlation with GC color is clear. This suggests that the total number of stars in a host GC is not an important factor in the formation of LMXBs.

Finally, we compare the luminosity function of the X-ray point sources matched with globular cluster candidates with those that are not matched with any optical source. Here, we study only the point sources within $1.5' < r < 6.0'$ of the center of NGC 4636, where the X-ray sources are not seriously contaminated by background AGN (see Figure 4). In Figure 16, we plot the LFs of GC-matched and non-GC matched X-ray point sources. There are approximately equal numbers in each category. The two plots represent X-ray luminosities obtained from two different epochs of observations, to account for the possible change in LF due to long term variability in these sources. The solid histogram shows the LF of the matched point sources, and the dashed histogram is the LF of all X-ray point sources that did not match a GC candidate. There is no difference between the slopes of the LFs of the GC sources and non-GC sources, and a Kolmogorov-Smirnov test reveals that both pairs of subsamples are drawn from the same parent

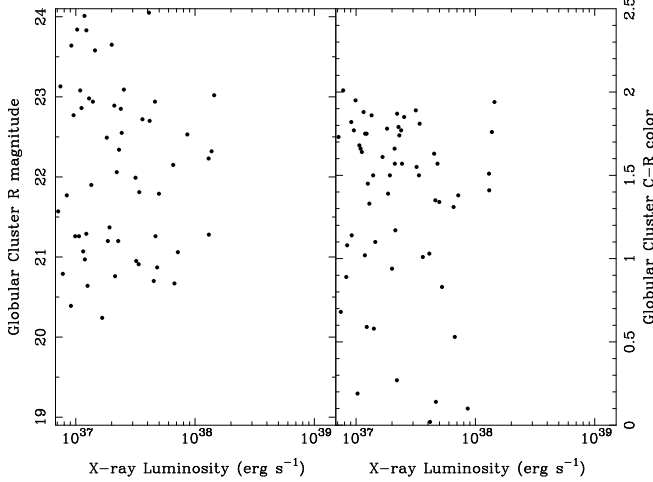


FIG. 15.— The mean X-ray luminosity of the point sources, with at least 10 counts and lying within $1.5' - 6'$ of the galactic center, that are found to match globular cluster candidates, plotted against the R magnitude (left) and the $C - R$ color (right) of the globular cluster candidates they are matched with. No trend is observed with the magnitude of the host globular cluster, while, as seen in Figure 14, the overabundance of matched X-ray sources in the redder GCs is easily apparent.

sample. Note, however, that the three brightest X-ray sources are not matched with any GC candidate.

3.5. Individual Sources

3.5.1. Galactic Nucleus

We detect a soft, luminous ($L_x = 2.1 \times 10^{38}$ erg s $^{-1}$) X-ray point source at the galaxy's nucleus, as determined from the VLA radio position ($\alpha(J2000) = 190.7077$, $\delta(J2000) = 2.6878$). This source is shown with an asterisk in the color-color diagram (Figure 5) and is significantly softer than the LMXBs. The spectrum is well-fit by a power-law model with a photon index of $\lambda = 2.36$ (1σ confidence range is $1.94 - 2.76$). Loewenstein et al. (2001) do not find nuclear activity in NGC 4636 in the 2 – 10 keV band. However, this source is very soft, and the $\sim 90\%$ of its emission falls below the 2 – 10 keV band.

3.5.2. Additional Black Hole Candidates

We detected two soft, luminous ($L_x \approx 1 \times 10^{38}$ erg s $^{-1}$) sources very near the center of the galaxy ($d < 0.1'$), whose soft spectra, like the source at the nucleus, may be signatures of black holes. McClintock & Remillard (2004) find that black hole binaries in the thermal-dominant state are well-described by a disk-blackbody model with $T = 1$ keV. These sources are shown by triangles in the color-color diagram (Figure 5). The spectra of these two sources are very similar, so we added them before fitting in XSPEC. With a disk-blackbody model, we find a best-fit temperature of 0.30 keV with a 1σ confidence range of 0.27 – 0.33 keV. The co-added spectra are equally well-fit by a power-law model with a photon index of $\lambda = 2.81$ (1σ confidence range 2.58 – 3.03). These sources do not vary in intensity during the observations.

Although we are prevented by the insufficient source counts from reaching a definitive conclusion, it is possible that these sources, and the one at the nucleus, are indeed signatures of black holes at the center of NGC 4636. If so, they may be massive black holes which fell to the galaxy center under dynamical friction, in which case they would have masses greater than $10^5 M_\odot$ (Tremaine & Ostriker 1999). However,

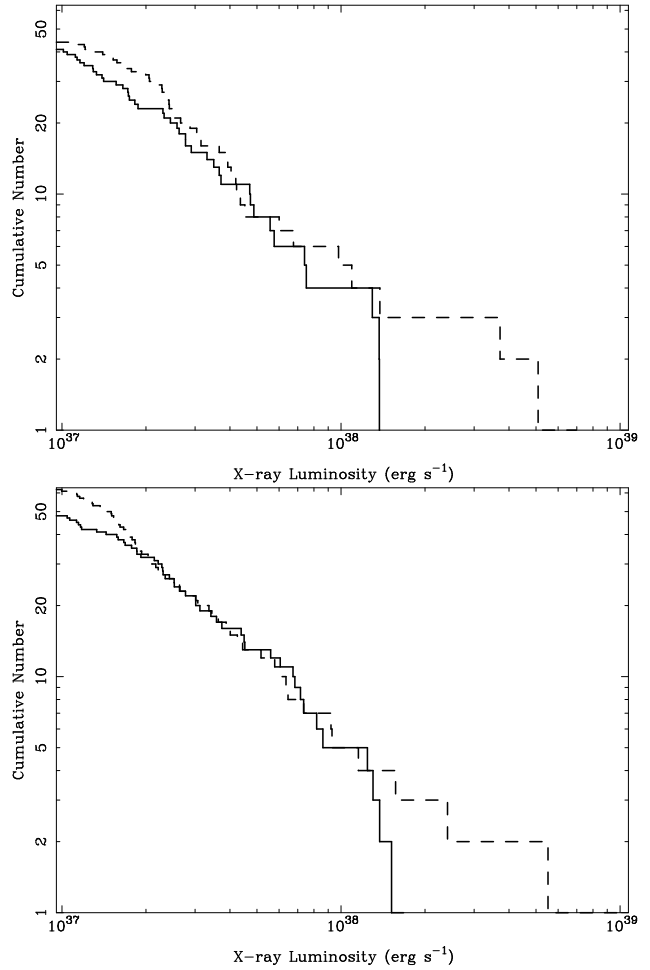


FIG. 16.— The luminosity function (LF) of all X-ray point sources, found within $1.5' < r < 6.0'$ of the center of NGC 4636 that are matched with globular cluster candidates brighter than $R < 23.5$ (solid histogram). Also plotted is the luminosity function of all X-ray point sources that did not match a GC candidate (dashed histogram). The two plots are for luminosities calculated for the Sequence 600083 observation (top) and the combined 600300 and 600331 observations (bottom). There is no difference between the slopes of the LFs of the GC sources and the non-GC sources. Note that the three brightest X-ray sources are not matched with globular clusters.

given the luminosities of these three sources, it is more likely that they formed near the center from a merger, with cooling gas triggering star formation.

3.5.3. SN 1939A

SN 1939A is a Type Ia supernova near the center of NGC 4636 ($\alpha(J2000)=190.700^\circ$, $\delta(J2000)=2.683^\circ$, distance from the center is $0.54'$). We do not detect X-ray emission at this location. By generating a large number of Poisson realizations from the observed background at this location in our *Chandra* observations, we calculate a 3σ X-ray count rate upper limit of 3.6×10^{-4} cts s $^{-1}$ in the 0.5 – 2 keV band. This translates to a luminosity upper limit of $\sim 4.3 \times 10^{37}$ erg s $^{-1}$ in the same energy band.

3.5.4. Bursting X-ray Source

A light curve for the bursting X-ray source, detected at $\alpha(J2000)=190.8821^\circ$, $\delta(J2000)=2.6193^\circ$, is shown in Figure 9. However, the source is approximately $11.4'$ from the center of the galaxy, and has an optical and near IR counter-

part too bright to be a member of NGC 4636. This source is probably a relatively nearby flare star in our Galaxy.

Figure 17 shows hard and soft band lightcurves for this source from the ACIS-S observation. No hard (2 – 6 keV) counts are detected prior to the burst.

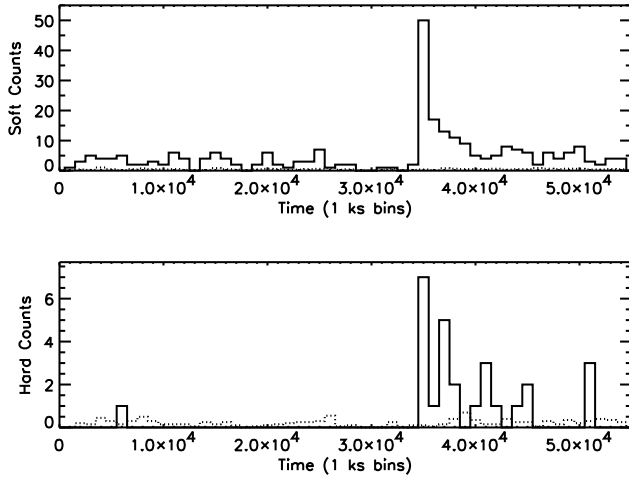


FIG. 17.— Soft band (0.3 – 2 keV, top panel) and hard band (2 – 6 keV, bottom panel) lightcurves from the ACIS-S observation for the bursting X-ray source at $\alpha(J2000) = 190.8821^\circ$, $\delta(J2000) = 2.6193^\circ$. Background counts are shown by the dotted line in each panel.

4. SUMMARY AND CONCLUSIONS

We have analyzed four *Chandra* ACIS observations, taken over three years and totaling ~ 210 ks, of the nearby Virgo galaxy NGC 4636, and have detected 245 X-ray point sources above a luminosity of 1×10^{37} erg s $^{-1}$ in the 0.5 – 2 keV band, outside the central 1.5' bright galaxy core. Based on the estimated AGN density in the field, ~ 120 of these are likely members of the galaxy, while the rest are likely AGN. In the

region from 1.5' to 6' from the center of the galaxy, there are 114 X-ray point sources detected with ≥ 10 counts, $\sim 20\%$ of which are likely AGN.

We calculate X-ray colors from fluxes (rather than from counts, as is traditionally done), and find that this results in more clearly grouped populations on the X-ray color-color diagram. We identify a large group of LMXBs, and a small group of much softer sources, including three within 6" of the galactic center which may be black holes.

We find 102 matches between our X-ray point sources and potential globular cluster (GC) candidates found in deep optical images of NGC 4636. Choosing the subset of 50 matched point sources with ≥ 10 raw counts, that correlate with GC candidates brighter than $R < 23.5$, and lie within $1.5' < r < 6'$ of the center of the galaxy (out of 114 X-ray point sources in this annulus), we find that the overwhelming majority are associated with the redder GC candidates, those that are thought to have near-solar metal abundance. However, we do not find any correlation between the abundance of point sources and the luminosity of the host GC candidate. The luminosity functions of the point sources matched with GCs and of those that are unmatched reveal similar underlying populations.

We searched for variable sources on timescales ranging from hours to years. We find that 51 sources in the common field of view (24%) show long-term variability and vary by $\geq 3\sigma$ between the January 2000 ACIS-S observation and the February 2003 ACIS-I observations, while only only 4 of the 87 sources (5%) in the two consecutive February 2003 ACIS-I observations show short-term variability, and of the 30 brightest sources in all observations, only four (13%) show significant variability during any one observation.

JPB thanks Vinay Kashyap for helpful discussions. This work was supported by NASA contracts NAS8-39073 and NAS8-03060, the Chandra Science Center, the Smithsonian Institution, and the University of Birmingham.

REFERENCES

Angelini, L., Loewenstein, M., & Mushotzky, R. F. 2001, ApJ, 557, L35
 Bauer, F.E. et al. 2004, ApJ, 128, 2048.
 Birkshaw, M., & Davies, R. L. 1985, ApJ, 291, 32
 Bregman, J. N. 2006, ArXiv Astrophysics e-prints, arXiv:astro-ph/0511635
 Buote, D. A. 2000, ApJ, 539, 172
 Dirsch, B., Schuberth, Y., & Richtler, T. 2005, A&A, 433, 43
 Dirsch, B., Richtler, T., Geisler, D., Forte, J. C., Bassino, L. P., & Gieren, W. P. 2003, AJ, 125, 1908
 Fabian, A. C., Pringle, J. E., & Rees, M. J. 1975, MNRAS, 172, 15P
 Forman, W., Jones, C., & Tucker, W. 1985, ApJ, 293, 102
 Gilfanov, M. 2004, MNRAS, 349, 146
 Grindlay, J. E. 1993, ASP Conf. Ser. 48: The Globular Cluster-Galaxy Connection, 48, 156
 Hut, P., et al. 1992, PASP, 104, 981
 Ivanova, N. 2006, ApJ, 636, 979
 Jones, C., Forman, W., Vikhlinin, A., Markevitch, M., David, L., Warmflash, A., Murray, S., & Nulsen, P. E. J. 2002, ApJ, 567, L115
 Jordán, A., et al. 2004, ApJ, 613, 279
 Knapp, G. R., Faber, S. M., & Gallagher, J. S. 1978, AJ, 83, 11
 Kundu, A., Maccarone, T. J., & Zepf, S. E. 2002, ApJ, 574, L5
 Loewenstein, M., Mushotzky, R., Angelini, L., & Arnaud, K. 2001, ApJ, 555, L21
 Loewenstein, M., & Mushotzky, R. 2003, Nuclear Physics B Proceedings Supplements, 124, 91
 Maccarone, T. J., Kundu, A., & Zepf, S. E. 2004, ApJ, 606, 430
 Matsushita, K., Makishima, K., Rokutanda, E., Yamasaki, N. Y., & Ohashi, T. 1997, ApJ, 488, L125
 McClintock, J. & Remillard, R. 2005, in Compact Stellar X-ray Sources, eds. W.H.G. Lewin and M. van der Klis (New York: Cambridge University Press)

Miles, T. A., Raychaudhury, S., Forbes, D. A., Goudfrooij, P., Ponman, T. J., & Kozhurina-Platais, V. 2004, MNRAS, 355, 785
 O'Sullivan, E., Vrtilek, J. M., & Kempner, J. C. 2005, ApJ, 624, L77
 Osmond, J. P. F., & Ponman, T. J. 2004, MNRAS, 350, 1511
 Prestwich, A., Irwin, J., Kilgard, R., Krauss, M., Zezas, A., Primini, F., Kaarat, P., & Boroson, B. 2003, ApJ, 595, 719
 Sandage, A. 1961, The Hubble Atlas of Galaxies (Washington, DC: CIW)
 Sarazin, C. L., Irwin, J. A., & Bregman, J. N. 2001, ApJ, 556, 533
 Sarazin, C. L., Kundu, A., Irwin, J. A., Sivakoff, G. R., Blanton, E. L., & Randall, S. W. 2003, ApJ, 595, 743
 Schuberth, Y., Richtler, T., Dirsch, B., Hilker, M., Larsen, S. S., Kissler-Patig, M., & Mebold, U. 2006, to appear in A&A, ArXiv Astrophysics e-prints, arXiv:astro-ph/0604309
 Swartz, D.A. et al. 2004, ApJS, 154, 519.
 Temi, P., Mathews, W. G., Brightenti, F., & Bregman, J. D. 2003, ApJ, 585, L121
 Tonry, J., Dressler, A., Blakeslee, J., Ajhar, E., Fletcher, A., Luppino, G., Metzger, M., & Moore, C. 2001, ApJ, 546, 681
 Tremaine, S., & Ostriker, J. P. 1999, MNRAS, 306, 662T
 Trinchieri, G., Kim, D.-W., Fabbiano, G., & Canizares, C. R. C. 1994, ApJ, 428, 555
 Vikhlinin, A. et al. 1995, ApJ, 451, 542V.
 White, R. E., Sarazin, C. L., & Kulkarni, S. R. 2002, ApJ, 571, L23
 Yoon S.-L., Yi S. K. & Lee Y.-W., to appear in Science (astro-ph/0601526)

TABLE 2
 SUMMARY OF X-RAY POINT SOURCES DETECTED IN NGC 4636

α (J2000)	δ (J2000)	Net Counts ^a	Luminosity ^a	Soft Color ^b	Hard Color ^c	Distance from Center (')	Notes ^d
190.7077	2.6878	202	2.144E+38	-0.37	-0.01	0.00	2
190.7091	2.6875	90	9.358E+37	-0.45	-0.14	0.08	3
190.7070	2.6865	69	1.025E+38	-0.39	-0.01	0.09	3
190.7061	2.6897	43	4.453E+37	-0.51	-0.06	0.15	3
190.7066	2.6910	88	9.199E+37	-0.58	-0.09	0.21	2 V
190.7017	2.6860	38	4.092E+37	0.20	0.40	0.38	2 V, GC 60
190.7066	2.6807	22	3.292E+37	-0.12	-0.35	0.43	1
190.7151	2.6860	11	1.625E+37	0.02	0.44	0.45	1
190.7159	2.6863	47	4.989E+37	0.08	0.50	0.50	2 V
190.7138	2.6788	14	2.035E+37	-0.04	0.59	0.65	1
190.7192	2.6851	12	1.715E+37	0.13	0.12	0.71	1
190.7136	2.6775	53	5.584E+37	0.15	0.48	0.71	2 V
190.7197	2.6885	47	4.905E+37	0.06	0.33	0.72	2 V
190.7189	2.6922	14	1.420E+37	-0.25	0.13	0.72	2 GC 78
190.7179	2.6943	12	1.760E+37	0.02	0.33	0.72	3
190.7148	2.6772	37	3.876E+37	-0.05	0.34	0.77	2
190.7140	2.6993	15	1.592E+37	-0.78	0.14	0.79	2 V
190.7226	2.6870	10	1.465E+37	0.03	0.51	0.89	1
190.7181	2.6767	14	1.470E+37	-0.61	0.23	0.91	2
190.6957	2.6974	43	4.623E+37	0.11	0.25	0.92	2
190.7173	2.7007	12	1.261E+37	-0.43	-0.30	0.96	2
190.7222	2.6769	19	1.956E+37	-0.67	-0.01	1.09	2
190.6881	2.6895	16	2.331E+37	0.01	0.11	1.18	1 GC 7
190.7249	2.6980	16	1.635E+37	-0.00	0.77	1.20	2 V
190.7282	2.6880	15	1.546E+37	-0.77	-0.48	1.23	3 GC 15
190.6877	2.6931	16	1.747E+37	0.59	-0.54	1.24	2 GC 73
190.7102	2.6672	33	3.532E+37	-0.09	0.12	1.25	2
190.6962	2.7053	17	2.494E+37	0.12	-0.16	1.25	1 V
190.6901	2.6992	32	4.768E+37	0.06	0.46	1.26	3
190.7294	2.6896	10	1.496E+37	-0.40	-0.04	1.30	3
190.7296	2.6895	28	4.175E+37	0.05	0.56	1.31	3
190.7212	2.6696	18	1.918E+37	-0.23	0.08	1.36	2 V
190.7295	2.6806	18	1.903E+37	-0.16	0.48	1.38	2 V
190.6844	2.6886	39	5.945E+37	-0.04	0.36	1.40	3 V
190.6831	2.6827	28	3.922E+37	0.09	0.37	1.51	3
190.7323	2.6763	28	4.041E+37	0.57	0.03	1.63	3
190.6977	2.6617	218	2.410E+38	-0.58	-0.31	1.68	3 V, GC 46
190.7091	2.7158	21	3.084E+37	0.04	0.57	1.68	3
190.7365	2.6859	11	1.680E+37	0.26	0.07	1.73	3
190.7366	2.6860	66	6.724E+37	0.05	0.48	1.74	3 V, GC 3
190.6785	2.6809	15	2.281E+37	0.05	0.52	1.80	3 GC 10
190.7367	2.6795	16	1.665E+37	0.07	0.72	1.81	2 V, GC 52
190.6785	2.6805	34	3.756E+37	0.02	0.55	1.81	3
190.6783	2.6979	20	2.335E+37	0.11	0.72	1.87	3 GC 12
190.7329	2.6690	15	1.573E+37	-0.02	0.68	1.88	2
190.6927	2.7157	10	1.066E+37	0.50	-0.18	1.90	2 GC 68
190.7132	2.6564	24	3.669E+37	0.26	0.39	1.91	3 V
190.6879	2.7132	60	6.465E+37	0.01	0.47	1.93	3
190.6779	2.7047	11	1.655E+37	-0.25	0.41	2.06	1
190.7097	2.7230	11	1.670E+37	-0.04	0.31	2.12	1 GC 37
190.6947	2.7209	13	1.371E+37	0.02	0.31	2.14	2 GC 66
190.7435	2.6858	19	2.882E+37	0.16	0.19	2.15	3
190.7225	2.6548	11	1.202E+37	0.16	0.10	2.17	3
190.7124	2.7237	14	2.122E+37	0.17	0.09	2.17	1 V
190.7398	2.7059	23	2.297E+37	0.09	0.69	2.21	2 V, GC 51
190.6906	2.7204	11	1.162E+37	0.10	0.57	2.21	3 GC 5
190.6725	2.7002	16	1.833E+37	0.14	0.24	2.24	2
190.7339	2.7155	16	1.592E+37	0.09	-0.12	2.29	2 V
190.6796	2.7138	12	1.746E+37	0.15	0.43	2.30	3
190.6717	2.6726	140	1.569E+38	0.09	0.45	2.35	3
190.7469	2.6804	20	2.036E+37	-0.03	0.33	2.39	3
190.6673	2.6818	40	5.994E+37	-1.09	-0.10	2.45	3 GC 28
190.6694	2.6722	82	1.094E+38	-0.06	0.29	2.48	3 GC 26
190.7021	2.7294	11	1.158E+37	0.08	0.08	2.52	2 GC 54
190.7401	2.6607	22	2.281E+37	0.04	0.61	2.53	3 GC 2
190.7452	2.6681	35	3.642E+37	0.07	0.53	2.54	3
190.7495	2.6799	23	2.429E+37	0.34	-0.32	2.55	2
190.6775	2.7210	74	8.203E+37	0.01	0.35	2.70	2 V, GC 79
190.7143	2.6431	136	1.519E+38	0.09	0.44	2.71	3
190.6776	2.7222	41	4.703E+37	0.10	0.51	2.74	3
190.6965	2.7322	21	2.259E+37	-0.05	0.53	2.75	2 V
190.6687	2.7118	36	4.019E+37	0.10	0.46	2.75	2 V, GC 90
190.6644	2.7046	28	3.122E+37	-0.01	0.46	2.79	2
190.7321	2.6476	17	2.587E+37	-0.02	0.66	2.82	3 GC 9
190.7263	2.6433	18	2.410E+37	0.17	-0.51	2.89	3

TABLE 2
SUMMARY OF X-RAY POINT SOURCES DETECTED IN NGC 4636

190.7549	2.6998	25	3.882E+37	0.16	0.41	2.92	1 GC 42
190.7556	2.6968	43	5.582E+37	0.12	0.37	2.92	3 GC 39
190.6600	2.6976	24	3.672E+37	0.01	0.39	2.93	3
190.7573	2.6914	11	1.733E+37	0.19	-0.22	2.98	1 V
190.7345	2.6447	10	1.565E+37	0.12	0.20	3.05	3 GC 8
190.7498	2.6591	237	3.728E+38	0.11	0.48	3.05	3 V, GC 43
190.6568	2.6925	27	3.319E+37	0.10	0.44	3.07	3
190.7207	2.6369	103	1.157E+38	-0.50	-0.34	3.15	3
190.6807	2.6414	60	7.519E+37	0.06	0.26	3.22	3
190.6738	2.6461	81	9.283E+37	0.04	0.53	3.23	3 V, GC 21
190.6579	2.6658	16	2.507E+37	-0.05	0.80	3.27	1
190.7039	2.6310	16	2.447E+37	-0.14	0.29	3.42	3
190.7647	2.6844	21	2.631E+37	0.09	0.36	3.42	3
190.7617	2.6691	12	1.294E+37	0.38	0.29	3.43	2
190.7649	2.6897	59	7.403E+37	0.15	0.51	3.43	3
190.7653	2.6846	11	1.130E+37	-0.19	-1.39	3.46	3
190.6962	2.7444	22	3.055E+37	-0.58	0.13	3.47	3
190.6895	2.7432	11	2.777E+37	-0.04	0.32	3.50	1 V, GC 6
190.7204	2.6303	495	5.525E+38	-0.08	-0.16	3.53	3
190.7667	2.6855	17	1.785E+37	0.06	0.55	3.54	2
190.7227	2.7457	51	5.172E+37	0.12	-0.14	3.59	2
190.7645	2.6686	17	2.769E+37	0.20	0.29	3.60	3
190.7687	2.7009	26	4.243E+37	0.09	0.43	3.74	3 GC 36
190.7678	2.6668	15	2.062E+37	0.12	0.26	3.82	3
190.7714	2.6875	25	2.583E+37	0.10	0.31	3.82	3
190.7625	2.6538	35	5.776E+37	0.07	0.45	3.87	1
190.6610	2.7331	18	2.105E+37	-0.14	0.17	3.91	2 GC 95
190.7429	2.6327	20	3.146E+37	-0.02	0.40	3.92	3
190.7773	2.6984	14	2.305E+37	0.16	0.19	4.22	3
190.6769	2.7525	119	1.305E+38	0.12	0.37	4.30	3 GC 20
190.7553	2.7417	73	7.349E+37	0.19	0.32	4.31	3 GC 41
190.7607	2.6384	10	1.054E+37	-1.04	-0.94	4.35	2 GC 88
190.7794	2.6747	18	1.921E+37	0.10	0.64	4.37	2
190.7132	2.7614	11	1.132E+37	0.70	-0.35	4.43	2
190.6341	2.6961	35	4.248E+37	0.05	0.55	4.45	2
190.7824	2.6848	15	1.561E+37	-0.21	0.15	4.48	2
190.6495	2.7350	26	3.022E+37	0.03	0.09	4.50	2
190.6790	2.7570	11	1.195E+37	0.07	0.74	4.50	2
190.6448	2.7309	16	1.858E+37	0.23	0.18	4.58	2
190.7470	2.7535	10	9.989E+36	0.11	0.48	4.59	2
190.6821	2.7600	53	5.797E+37	-0.05	-0.20	4.60	2
190.7002	2.7645	11	1.177E+37	0.14	0.45	4.62	2 GC 63
190.7056	2.7651	117	1.370E+38	0.09	0.51	4.64	3 GC 38
190.6667	2.7546	20	2.213E+37	-0.32	0.02	4.70	2
190.6925	2.7647	28	3.723E+37	0.12	0.42	4.71	3 GC 4
190.6435	2.7329	15	1.830E+37	0.04	0.25	4.71	2
190.7307	2.6123	53	6.034E+37	0.02	0.47	4.73	3
190.6293	2.6774	27	3.410E+37	-0.08	0.46	4.75	2
190.7077	2.6062	18	2.325E+37	0.03	0.59	4.89	3
190.7534	2.6180	16	1.855E+37	0.07	0.31	5.00	2
190.6768	2.7682	24	2.652E+37	0.07	0.51	5.17	3
190.6705	2.6098	29	4.744E+37	0.07	0.33	5.19	3
190.6228	2.7058	68	8.620E+37	0.04	0.44	5.21	2
190.6739	2.7684	14	1.504E+37	-0.81	-0.42	5.25	2 V
190.6949	2.7748	13	1.374E+37	0.21	0.71	5.28	2 GC 65
190.7300	2.7745	25	2.639E+37	0.07	0.31	5.37	2 V, GC 59
190.7488	2.6077	16	1.883E+37	0.36	0.03	5.40	2 GC 89
190.6632	2.6094	13	1.601E+37	0.11	0.59	5.41	3 GC 29
190.7174	2.7783	53	5.611E+37	0.31	0.23	5.46	3
190.7936	2.7205	131	1.377E+38	0.13	0.23	5.51	2
190.6609	2.7674	13	1.510E+37	0.10	0.65	5.54	2 GC 92
190.7187	2.7796	20	2.095E+37	-0.10	0.29	5.55	2 GC 80
190.6781	2.7756	56	6.753E+37	0.13	0.37	5.56	3 GC 11
190.7851	2.6360	23	2.531E+37	0.08	0.20	5.59	2
190.6721	2.7743	11	1.286E+37	-0.22	0.42	5.61	2 GC 87
190.7889	2.7349	16	1.715E+37	0.15	0.37	5.63	2 V
190.7838	2.6313	21	2.307E+37	0.16	0.26	5.68	2
190.7018	2.7826	23	2.527E+37	0.12	0.73	5.70	3
190.6351	2.7500	12	1.398E+37	-0.10	-0.08	5.74	2
190.6443	2.7595	37	4.509E+37	0.06	0.55	5.74	2
190.7403	2.7782	69	7.166E+37	0.03	0.40	5.76	2 V, GC 50
190.8046	2.6861	15	1.617E+37	-0.35	0.20	5.81	2
190.6636	2.7747	14	1.561E+37	0.19	0.34	5.85	2 GC 91
190.7139	2.5901	31	3.868E+37	0.01	0.34	5.87	3 GC 30
190.6753	2.7803	15	1.667E+37	0.21	0.11	5.88	2 GC 86
190.6508	2.6076	26	3.362E+37	0.05	0.44	5.90	2
190.7193	2.7863	32	3.459E+37	0.17	0.07	5.95	3

TABLE 2
SUMMARY OF X-RAY POINT SOURCES DETECTED IN NGC 4636

190.7947	2.6365	58	6.524E+37	0.06	0.54	6.06	2
190.6770	2.7844	56	6.355E+37	-0.19	-0.22	6.08	3 GC 19
190.6589	2.7769	48	5.590E+37	-0.52	-0.06	6.10	3
190.6698	2.7821	15	1.679E+37	0.01	-0.09	6.10	2
190.7318	2.5880	14	1.798E+37	0.08	0.73	6.16	2 GC 58
190.7816	2.6161	21	2.391E+37	0.21	0.00	6.17	2
190.8104	2.6704	105	1.152E+38	0.18	0.39	6.25	2 GC 57
190.6502	2.6008	12	1.563E+37	0.32	0.29	6.26	3
190.6987	2.5836	73	1.447E+38	-0.00	0.35	6.28	3
190.7202	2.7919	207	3.033E+38	0.02	0.22	6.29	3
190.7666	2.7749	24	5.081E+37	-0.04	0.06	6.31	3
190.6516	2.7772	153	1.819E+38	-0.42	0.07	6.33	2 GC 47
190.7753	2.7701	79	8.329E+37	0.19	0.58	6.39	3 GC 33
190.6098	2.6428	61	8.421E+37	0.14	0.24	6.47	2
190.6830	2.7928	18	2.070E+37	0.06	-0.14	6.47	2 V
190.7156	2.7964	11	1.265E+37	-0.07	-1.15	6.53	2
190.7126	2.5783	16	2.643E+37	0.47	-0.42	6.58	1
190.7130	2.8005	200	2.232E+38	0.04	0.35	6.77	3 V
190.8140	2.7262	71	7.669E+37	0.01	0.31	6.78	2 GC 56
190.7639	2.5887	26	3.157E+37	-0.02	0.48	6.83	2
190.7948	2.7633	141	1.525E+38	0.00	0.40	6.92	3
190.7406	2.5757	25	3.160E+37	0.08	0.35	7.01	2 GC 94
190.7424	2.7994	33	3.591E+37	0.17	0.30	7.01	3 GC 1
190.8259	2.7029	38	4.197E+37	0.11	0.62	7.14	2
190.7296	2.5706	11	3.494E+37	-0.20	0.38	7.15	1 V
190.7417	2.8036	57	6.271E+37	0.13	0.36	7.24	2 V
190.7409	2.5706	25	7.828E+37	-0.18	0.35	7.31	1
190.7458	2.5699	18	5.708E+37	-0.33	0.61	7.43	1 V
190.7077	2.8149	15	1.743E+37	-0.08	-1.21	7.62	2 GC 97
190.7626	2.5723	18	2.182E+37	0.01	1.11	7.67	2
190.7627	2.5709	25	3.136E+37	0.02	0.52	7.75	2 GC 81
190.8375	2.7035	35	9.525E+37	0.08	0.54	7.84	3
190.7227	2.8181	109	1.238E+38	0.04	0.35	7.87	3 V, GC 18
190.7455	2.8144	19	2.085E+37	0.24	0.64	7.93	2
190.8044	2.7805	25	2.750E+37	-0.05	0.41	8.03	2
190.8405	2.6687	13	4.232E+37	0.15	0.31	8.05	1
190.7859	2.7983	70	7.572E+37	0.15	0.36	8.12	2
190.8365	2.6456	37	4.316E+37	0.25	0.47	8.13	2
190.7980	2.7892	29	3.165E+37	0.10	0.64	8.15	2 GC 64
190.7694	2.8093	89	1.058E+38	0.10	0.08	8.17	3 GC 35
190.6818	2.8229	20	2.454E+37	0.10	0.84	8.26	2 V
190.8465	2.6914	26	3.009E+37	-0.02	0.55	8.33	2
190.8178	2.6007	11	1.313E+37	0.11	0.87	8.42	2
190.8511	2.6851	49	5.654E+37	0.05	-0.13	8.60	2 V, GC 98
190.8525	2.6938	62	7.281E+37	0.16	0.46	8.69	2
190.7616	2.8226	149	1.711E+38	0.13	0.36	8.71	3
190.7128	2.8330	47	5.811E+37	0.16	0.49	8.71	3 GC 32
190.6729	2.8288	25	7.669E+37	0.12	0.39	8.72	1
190.6726	2.8298	77	9.604E+37	0.09	0.57	8.78	2
190.7304	2.8324	446	6.158E+38	0.03	0.21	8.78	3
190.8027	2.5760	37	1.289E+38	0.12	0.33	8.80	3 V
190.7845	2.5613	129	1.689E+38	0.02	0.37	8.88	2
190.6497	2.8264	23	2.901E+37	0.10	0.30	9.02	2 GC 49
190.7927	2.5634	13	1.663E+37	-0.44	0.32	9.04	2
190.7492	2.8341	54	6.379E+37	0.07	0.49	9.12	2
190.8596	2.7028	16	5.307E+37	-0.05	0.21	9.15	1
190.8599	2.7040	24	2.831E+37	-0.08	0.38	9.18	2
190.8533	2.7453	365	4.294E+38	0.00	0.34	9.39	3 V
190.6858	2.8436	30	3.753E+37	0.19	0.41	9.44	2 V, GC 74
190.8316	2.5905	28	3.591E+37	0.11	0.50	9.45	2 V
190.7257	2.8446	13	1.536E+37	-1.55	-4.34	9.47	2 GC 69
190.8316	2.5894	32	1.099E+38	-0.21	0.03	9.49	1 V
190.8314	2.7906	36	4.184E+37	0.20	0.47	9.65	2 GC 55
190.8421	2.7801	23	2.697E+37	0.16	0.17	9.78	2 GC 102
190.8517	2.6100	69	8.833E+37	0.11	0.47	9.82	2
190.8519	2.6091	21	7.219E+37	0.26	0.35	9.86	1
190.7904	2.8303	17	1.978E+37	0.11	0.50	9.88	2
190.8727	2.6895	27	3.332E+37	0.10	0.33	9.90	2
190.7947	2.8286	54	6.317E+37	0.03	0.43	9.93	2
190.7280	2.8528	47	5.751E+37	0.12	0.45	9.97	2
190.7955	2.8292	22	6.468E+37	0.12	0.09	9.98	1
190.7587	2.8470	52	6.201E+37	0.12	0.39	10.03	2
190.7279	2.8544	73	9.046E+37	0.26	0.30	10.07	3
190.6929	2.8560	19	2.482E+37	0.26	0.40	10.13	2
190.8665	2.6105	30	3.922E+37	-0.06	-0.70	10.59	2 V
190.7280	2.8655	16	2.070E+37	-0.22	0.23	10.73	2 GC 61
190.8797	2.7403	170	2.121E+38	0.06	0.47	10.78	3 V

TABLE 2
SUMMARY OF X-RAY POINT SOURCES DETECTED IN NGC 4636

190.8569	2.5829	17	2.215E+37	0.15	0.17	10.94	2
190.8177	2.8340	261	3.208E+38	-0.03	0.26	10.97	3 V
190.8910	2.6651	24	8.049E+37	-0.06	0.46	11.08	1
190.8288	2.5476	13	4.558E+37	-0.03	0.76	11.11	1
190.8922	2.6655	67	8.661E+37	0.06	0.38	11.15	2
190.8774	2.6113	14	1.945E+37	-0.21	0.42	11.17	2
190.8820	2.6193	147	1.966E+38	-0.28	-0.03	11.24	2 V, GC 85
190.8825	2.6193	216	2.890E+38	-2.22	-0.48	11.26	2 V, GC 84
190.8828	2.6184	140	4.889E+38	-0.32	0.05	11.30	1 V
190.8649	2.7920	64	7.898E+37	0.17	0.70	11.31	2 V
190.8655	2.7925	69	8.685E+37	-0.19	1.04	11.36	2 V
190.8587	2.5711	13	1.997E+37	-0.37	0.53	11.45	2
190.8905	2.6303	17	5.940E+37	0.33	0.45	11.50	1 V, GC 13
190.8679	2.8009	39	5.002E+37	0.21	0.28	11.76	2
190.8582	2.5554	15	2.330E+37	-0.08	0.53	12.03	2
190.9019	2.7936	26	3.577E+37	0.13	0.44	13.27	2

^a Net counts and luminosity (erg s⁻¹) are in the 0.5 – 2 keV band.

^b Soft color is defined as (M-S)/(S+M+H) where S, M, and H are the fluxes in bands 0.5 – 1, 1 – 2, and 2 – 8 keV, respectively.

^c Hard color is defined as (H-M)/(S+M+H) where S, M, and H are the fluxes in bands 0.5 – 1, 1 – 2, and 2 – 8 keV, respectively.

^d 1 means the source was detected by the ACIS-S, 2 means the source was detected by the ACIS-I, and 3 means the source was detected by both instruments. V denotes a long-term (i.e. between observations) variable and SV denotes a short-term (i.e. during a single observation) variable. GC indicates that the sources is matched with a globular cluster. The number following GC gives the source's position in Table 3.

TABLE 3
X-RAY POINT SOURCES MATCHED WITH GLOBULAR CLUSTERS CANDIDATES IN NGC
4636

N	R.A. (X-ray)	Dec (X-ray)	Offset('')	CTIO ID ^a	R.A. (optical)	Dec (optical)	C-R color	R magnitude
1	190.7424	2.7994	0.57	6947	190.7422	2.7994	1.13	22.29
2	190.7401	2.6607	1.31	11690	190.7399	2.6610	0.94	23.65
3	190.7366	2.6860	0.90	13857	190.7368	2.6862	1.57	20.87
4	190.6925	2.7647	0.49	1033	190.6925	2.7649	1.50	20.91
5	190.6906	2.7204	0.33	5983	190.6905	2.7204	1.88	21.07
6	190.6895	2.7432	0.82	5961	190.6893	2.7433	1.50	22.94
7	190.6881	2.6895	0.87	13558	190.6882	2.6897	1.25	21.70
8	190.7345	2.6446	0.70	13847	190.7346	2.6448	1.75	20.97
9	190.7321	2.6476	0.80	6764	190.7319	2.6477	1.17	20.76
10	190.8943	2.5651	1.34	1825	190.8946	2.5652	1.06	24.24
11	190.6807	2.6414	0.88	5760	190.6809	2.6416	1.38	21.06
12	190.6796	2.7138	0.38	5739	190.6796	2.7139	1.45	20.64
13	190.6785	2.6805	0.44	5720	190.6786	2.6804	1.01	22.72
14	190.6776	2.7222	0.80	5705	190.6778	2.7223	1.35	22.94
15	190.7296	2.6895	0.51	13824	190.7296	2.6896	1.45	23.36
16	190.7294	2.6896	0.77	13824	190.7296	2.6896	1.45	23.36
17	190.7282	2.6880	0.92	11611	190.7283	2.6878	-0.37	24.27
18	190.7243	2.6197	0.92	1166	190.7242	2.6199	0.58	24.64
19	190.7225	2.6548	0.94	6579	190.7223	2.6546	1.02	24.01
20	190.6779	2.7047	1.38	960	190.6783	2.7049	1.82	20.39
21	190.7211	2.7122	0.52	11565	190.7210	2.7123	1.95	21.26
22	190.6769	2.7525	0.05	953	190.6769	2.7525	1.51	22.23
23	190.6705	2.6098	1.38	13483	190.6708	2.6099	0.02	22.70
24	190.8533	2.7453	0.83	1707	190.8533	2.7455	0.75	20.30
25	190.8316	2.5894	1.30	8368	190.8316	2.5898	2.07	22.26
26	190.7202	2.7919	0.62	1150	190.7201	2.7919	0.50	19.63
27	190.7193	2.7105	0.66	6526	190.7193	2.7107	0.68	23.13
28	190.7192	2.6851	0.50	6525	190.7192	2.6853	1.55	20.41
29	190.7186	2.6933	0.21	16230	190.7186	2.6932	3.89	22.56
30	190.6600	2.6976	0.89	5431	190.6600	2.6978	1.55	20.95
31	190.7174	2.7783	0.27	11548	190.7173	2.7783	0.83	24.52
32	190.7162	2.6995	0.97	6477	190.7165	2.6996	2.07	21.02
33	190.6568	2.6925	0.61	13398	190.6569	2.6926	1.89	21.99
34	190.7143	2.6431	0.93	6444	190.7143	2.6434	1.94	23.02
35	190.7138	2.6788	0.56	15524	190.7138	2.6789	1.91	22.15
36	190.6502	2.6008	1.47	15478	190.6505	2.6005	0.31	23.04
37	190.7773	2.6984	0.75	7545	190.7771	2.6983	1.78	22.49
38	190.7653	2.6846	1.15	15737	190.7650	2.6846	1.66	23.08
39	190.7649	2.6897	1.09	1372	190.7646	2.6898	0.53	20.67
40	190.7647	2.6844	0.53	15298	190.7646	2.6845	1.77	22.85
41	190.7645	2.6686	0.42	7355	190.7646	2.6686	1.66	22.89
42	190.7625	2.6538	0.91	1369	190.7624	2.6540	1.31	22.15
43	190.7616	2.8226	0.54	11809	190.7615	2.8228	-0.23	22.64
44	190.7573	2.6914	0.98	7234	190.7572	2.6917	1.65	23.90
45	190.7077	2.6062	1.39	1098	190.7080	2.6065	1.79	21.20
46	190.7067	2.7285	1.01	11489	190.7068	2.7288	2.01	20.79
47	190.7056	2.7651	0.55	6281	190.7057	2.7652	1.41	21.28
48	190.7556	2.6968	0.58	7203	190.7555	2.6969	1.34	21.79
49	190.7552	2.6312	0.54	7201	190.7553	2.6313	1.64	22.86
50	190.7053	2.6799	1.41	13675	190.7049	2.6798	0.94	20.65
51	190.7039	2.6310	0.48	15699	190.7039	2.6309	1.57	25.02
52	190.7018	2.7826	1.03	14741	190.7018	2.7829	0.27	24.73
53	190.6228	2.7058	0.24	4797	190.6228	2.7057	0.10	22.53
54	190.7936	2.7206	0.17	1482	190.7935	2.7206	1.76	22.32
55	190.7845	2.5613	0.16	7666	190.7846	2.5613	0.03	22.12
56	190.7403	2.7782	0.26	1255	190.7402	2.7781	1.03	24.05
57	190.7398	2.7059	0.54	15278	190.7397	2.7058	0.59	23.83
58	190.6451	2.6996	0.69	13364	190.6450	2.6994	0.19	23.84
59	190.7339	2.7155	1.47	15274	190.7337	2.7158	0.89	24.39
60	190.6448	2.7309	0.52	5145	190.6447	2.7308	1.39	21.20
61	190.7332	2.7029	0.44	11643	190.7330	2.7029	1.71	23.14
62	190.6443	2.7595	0.65	5133	190.6441	2.7594	1.63	20.70
63	190.7329	2.6690	0.14	6780	190.7329	2.6689	1.77	22.77
64	190.6293	2.6774	1.37	4905	190.6289	2.6774	1.81	21.81
65	190.8314	2.7906	0.30	1615	190.8314	2.7906	1.24	23.67
66	190.8259	2.7029	1.00	8282	190.8256	2.7028	0.20	21.40
67	190.8140	2.7262	0.86	8118	190.8139	2.7260	1.30	22.18
68	190.7318	2.5880	1.21	1215	190.7315	2.5881	1.61	20.06
69	190.7300	2.7745	0.71	6707	190.7298	2.7744	1.86	21.90
70	190.5945	2.8599	0.77	4352	190.5947	2.8599	0.11	22.10
71	190.5901	2.8303	0.60	10851	190.5900	2.8304	0.92	21.81
72	190.7002	2.7645	0.51	1065	190.7002	2.7646	1.33	22.98
73	190.6982	2.6963	1.10	1059	190.6983	2.6960	1.04	21.76
74	190.8044	2.7805	0.74	7973	190.8044	2.7803	0.02	22.51
75	190.7980	2.7892	0.33	7866	190.7981	2.7891	1.58	21.41

TABLE 3
X-RAY POINT SOURCES MATCHED WITH GLOBULAR CLUSTERS CANDIDATES IN NGC
4636

76	190.7947	2.6365	0.93	7822	190.7945	2.6364	1.74	21.86
77	190.6942	2.7729	0.80	6052	190.6940	2.7728	1.73	21.57
78	190.7269	2.7077	1.01	6655	190.7267	2.7076	1.08	21.77
79	190.6927	2.7157	0.75	13583	190.6925	2.7155	1.68	21.26
80	190.7257	2.8446	0.89	11588	190.7258	2.8444	1.17	20.44
81	190.7851	2.6360	1.00	7670	190.7850	2.6358	1.85	23.09
82	190.7838	2.6313	0.61	7652	190.7839	2.6312	1.74	22.34
83	190.7794	2.6748	0.63	1435	190.7794	2.6746	1.50	21.37
84	190.6877	2.6931	0.61	13554	190.6877	2.6929	1.29	22.87
85	190.7249	2.6980	0.53	6619	190.7248	2.6978	1.66	21.46
86	190.7231	2.6154	0.35	11574	190.7231	2.6153	1.75	21.29
87	190.7669	2.7410	1.38	7388	190.7665	2.7408	1.66	20.39
88	190.6775	2.7210	0.84	5692	190.6772	2.7210	0.14	21.26
89	190.7627	2.5709	1.22	7325	190.7623	2.5709	2.02	24.12
90	190.8922	2.6655	0.94	1819	190.8922	2.6653	1.34	23.83
91	190.6753	2.7803	0.30	5651	190.6752	2.7803	1.61	20.24
92	190.8774	2.6113	0.22	8933	190.8775	2.6113	0.93	22.66
93	190.7173	2.7007	0.71	13743	190.7172	2.7005	0.64	22.69
94	190.7534	2.6180	1.35	7170	190.7536	2.6177	1.10	23.58
95	190.7495	2.6799	0.25	7081	190.7495	2.6799	1.57	22.55
96	190.7492	2.8341	1.18	13910	190.7489	2.8339	1.36	23.23
97	190.6699	2.6470	0.13	918	190.6699	2.6469	1.27	21.70
98	190.6644	2.7046	0.55	11250	190.6643	2.7046	1.87	22.06
99	190.8665	2.6105	1.02	8799	190.8663	2.6102	0.23	22.20
100	190.8599	2.7040	0.80	12312	190.8599	2.7038	0.22	22.71
101	190.8511	2.6851	0.87	8613	190.8510	2.6849	0.02	24.12
102	190.8421	2.7801	0.60	1655	190.8422	2.7800	1.07	19.72

^a Dirsch et al. 2005